JAAS

Accepted Manuscript

This is an *Accepted Manuscript*, which has been through the Royal Society of Chemistry peer review process and has been accepted for publication.

Accepted Manuscripts are published online shortly after acceptance, before technical editing, formatting and proof reading. Using this free service, authors can make their results available to the community, in citable form, before we publish the edited article. We will replace this *Accepted Manuscript* with the edited and formatted *Advance Article* as soon as it is available.

You can find more information about *Accepted Manuscripts* in the Information for Authors.

Please note that technical editing may introduce minor changes to the text and/or graphics, which may alter content. The journal's standard Terms & Conditions and the Ethical guidelines still apply. In no event shall the Royal Society of Chemistry be held responsible for any errors or omissions in this *Accepted Manuscript* or any consequences arising from the use of any information it contains.

ROYAL SOCIETY OF CHEMISTRY

www.rsc.org/jaas

Three-Dimensional Elemental Imaging of Li-ion Solid-State Electrolytes Using fs-Laser Induced Breakdown Spectroscopy (LIBS)

Huaming Hou,[a,b] Lei Cheng,[a,c] Thomas Richardson,[a] Guoying Chen,[a] Marca Doeff,[a] Ronger Zheng,[b] Richard Russo[a,d] and Vassilia Zorba[a,*]

[a] *Lawrence Berkeley National Laboratory, Berkeley, CA 94720, USA.*

[b] *Optics and Optoelectronics Laboratory, Ocean University of China, Qingdao 266100,China.*

[c] *Department of Material Sciences and Engineering, University of California, Berkeley, CA 94720, USA.*

[d] *Applied Spectra, 46661 Fremont Blvd., Fremont, CA 94538, USA.*

Abstract

Direct chemical imaging is critical to understand and control processes that affect the performance and safety of Li-ion batteries. In this work, femtosecond-Laser Induced Breakdown Spectroscopy (fs-LIBS) is introduced for 3D chemical analysis of Li-ion solid state electrolytes in electrochemical energy storage systems. Spatially resolved chemical maps of major and minor elements in solid-state electrolyte $Li_7La_3Zr_2O_{12}$ (LLZO) samples are presented, with a depth resolution of 700 nm. We implement newly-developed visualization techniques to chemically image the atomic ratio distributions in an LLZO solid-state electrolyte matrix. Statistical analysis, 2D layer-by-layer analysis, 2D cross-sectional imaging and 3D reconstruction of atomic ratios are demonstrated for electrolyte samples prepared under different processing conditions. These results explain the differences in the physical properties of the samples not revealed by conventional characterization techniques, and demonstrate the ability of fs-LIBS for direct 3D elemental imaging of Li-ion battery solid-state electrolytes.

Corresponding author: VZormpa@lbl.gov

1. Introduction

Rechargeable lithium-ion (Li-ion) batteries are the most widely used energy storage technology for consumer electronics and the most promising option for large format applications such as electric vehicles due to their high specific energies and good cycle lives. However, Li-ion batteries suffer from an array of safety issues due to the flammability and leakage of the organic electrolytic solutions used in them. Using a solid electrolyte obviates these issues and may enable reliable cycling of lithium metal anodes, resulting in higher energy density devices than those that utilize graphite negative electrodes.

Several lithium ion conducting solid electrolytes have been proposed for use in solid state batteries.[1] The stuffed lithium garnet $Li_7La_3Zr_2O_{12}$ (LLZO), first reported by Weppner's group[2] in 2007, is considered one of the most promising candidates because of its high ionic conductivity and purported resistance to reduction by metallic lithium. LLZO has two polymorphs, cubic and tetragonal, and it has been shown that the cubic variant has an ionic conductivity several orders of magnitude higher than that of the tetragonal structure.[3] There are several benefits to partial Al-substitution in LLZO, the foremost being that it stabilizes the cubic structure.[4,5] It is thought that the creation of Li vacancies, while maintaining the oxygen stoichiometry, is necessary to stabilize cubic LLZO.[6] A second benefit is the fact that a small amount of Al added to LLZO can greatly accelerate densification during the sintering process.[7,8] Nevertheless, even Al-substituted LLZO normally requires long sintering at temperatures of at least 1100°C to ensure densification.[9] This inevitably results in loss of lithium and significant nonstoichiometry in the densified material.[7] On the other hand, the addition of Al can also lead to new impurity phases, chemical composition changes, and element distribution gradients at surfaces, grain boundaries, and in the bulk of LLZO pellets.[7] Because of their low levels and the distribution patterns, the impurities are often difficult or impossible to detect by conventional characterization techniques such as x-ray diffraction, but they still may greatly affect the electrochemical properties. For example, the dominant contributor to the internal resistance in all-solid-state lithium batteries may not be the bulk resistance of the solid electrolyte, but the interfacial resistance between the electrodes and solid electrolytes. In LLZO, this is strongly related to surface composition, elemental

distribution, and impurity segregation.[9–11] Thus, analysis of the chemical distribution at the electrolyte surfaces relative to the bulk is critical to the optimization of these materials for use in practical electrochemical devices.

Control and reproducibility of the desired atomic ratio distribution is therefore required, not only at the interface but also in the LLZO material bulk. Bulk chemical compositions of Al-substituted LLZO has been previously studied using ICP-OES (Inductively Coupled Plasma – Optical Emission Spectroscopy),[3–5,12] ICP-MS (Inductively Coupled Plasma – Mass Spectroscopy), and LA-ICP-MS[4] (Laser Ablation Inductively Coupled Plasma Mass Spectroscopy), but these techniques do not provide any spatially-resolved information. EDS (Energy-Dispersive X-ray Spectroscopy) has often been used to study the surface elemental distribution of Al, La and Zr in LLZO.[4,6,13] However, Li cannot be directly detected with this method,[4] and matrix effects can affect the apparent composition due to variations in the X-ray penetration depth.[7] These issues leave a pressing need for the development of versatile spatially resolved 3D techniques with high sensitivity for elemental analysis of Li-ion containing materials.

Laser Induced Breakdown Spectroscopy (LIBS) is an atomic emission spectroscopy technique that is based on the detection of spectral emission from a luminous plasma produced upon the interaction of an intense laser pulse with a material.[14–17] LIBS allows bulk analysis as well as depth profiling, surface chemical mapping, and layer-by-layer analysis, all at atmospheric pressure conditions.[18–23] While nanosecond (ns) lasers are commonly used for material sampling,[24,25] femtosecond (fs) lasers are more suitable for spatially- and depth-resolved chemical analysis because of the confined nature of the fs laser-material interaction associated with suppressed thermal effects.[26,27] As a result, femtosecond LIBS axial (depth) resolutions of nanometers/pulse have been demonstrated,[28,29] while lateral resolution can scale down to the sub-micrometer range.[30–32]

In this work we adopted fs-LIBS to chemically image solid-state lithium-ion LLZO ($Li_7La_3Zr_2O_{12}$) electrolytes. The distributions and atomic ratios of major (Li, La, Zr) and minor (Al) elements in Al-substituted LLZO samples processed at different conditions were studied. 2D surface, 2D cross-sectional and newly developed visualization techniques for the 3D reconstruction of elemental distribution in LLZO matrices are demonstrated. This new application of fs-LIBS in 3D chemical imaging of solid-state

electrolytes in Li-ion battery systems opens up new possibilities for the use of LIBS in electrochemical energy storage systems.

2. Experimental

2.1 Materials and methods

Stoichiometric amounts of $La(OH)_3$ (Alfa 99.95% REO), ZrO_2(Aldrich 99%) and Li_2CO_3 (Aldrich >99.0%) with 2% w/w Al_2O_3 (Alcoa) were mixed in a zirconia vessel for 30 minutes by using a Spex SamplePrep 8000M mixer/mill. The LLZO powder was synthesized by heating the mixture to 1000 ℃ for 12 hours in a capped alumina tray in air and was then collected, ground and sieved. Part of the sieved LLZO powder was attrition milled in isopropyl alcohol (IPA) at 450 RPM for 2 hours and subsequently dried in air and collected for making dense pellets. The remaining sieved powder was used to cover pellets during sintering, with half of the powder further annealed in alumina crucibles at 1100 ℃ for another 6 hours before being used as a powder cover while the other half was used without further processing.

Compact pellets were cold uniaxially pressed from fresh milled powders without any binder. The pressed pellets were placed on powder beds in capped alumina trays and fully covered by either of the two different LLZO powders (fresh and 6 hour annealed). The resulting LLZO pellets are referred to as LLZO_0h and LLZO_6h, respectively from this point on. Finally, the two samples were fired at 1100 ℃ for 12 hours in air. Detailed sample preparation can be found in our previous report.[9]

2.2 3D elemental imaging with fs-LIBS

A frequency tripled (343 nm) diode-pumped Ytterbium femtosecond laser (s-pulse, Amplitude Systems) was used as the excitation source, delivering 500 fs pulses at a repetition rate of 5 Hz. The fs-laser beam was focused on a sample surface by a UV microscope objective lens. Spatially resolved 3-D chemical imaging with LIBS was achieved by scanning the sample across 3-axes (x,y,z) with respect to the femtosecond laser beam using high-precision motorized stages. Neutral density filters were used to attenuate the fs-laser beam and control the exact amount of laser energy (160 μJ). The laser-induced plasma optical emission was imaged onto an optical fiber bundle by using

UV fused silica plano-convex lenses, and the fiber was directly connected to the slit entrance of a Czerny Turner spectrometer (1200 gr/mm)/ICCD (Acton 2150/Princeton Instruments) camera system. The gate of the ICCD camera was triggered by the fs-laser and the relative delay was controlled by the ICCD.

An area of 1.11×1.11 mm^2 was chemically mapped by laser sampling over a 15×15 grid, with every ablation location generated by a sequence of 50 pulses to produce 50 layer-by-layer maps. The integrated emission intensity of the LIBS emission lines for each of the 11,250 ($50 \times 15 \times 15$) locations per sample were measured and subsequently assigned to xyz space coordinates. These were in turn used to construct contour maps of each layer (across each lateral plane) and depth profiling contours across each selected axial plane. Home-built data processing algorithms were used for data management and spatial allocation (Matlab). Stacks of 2D cross-sectional elemental ratio maps (depth) were implemented to produce volume images using image-processing software (Amide). Following chemical imaging the topologies of the samples were studied using white-light interferometry (Zygo-Multiview 6K). The bulk chemical composition of LLZO_0h was determined using ICP-OES, and served as a standard for quantification with fs-LIBS. A Perkin-Elmer Optima 5400 inductively coupled plasma optical emission spectrometer was used to obtain bulk chemical compositions.

3. Results and Discussion

3.1 Laser sampling and construction of elemental ratio maps

Fig. 1a and **c** show white-light interferometry images of LLZO_0h and LLZO_6h respectively for femtosecond laser ablation sampling with a total of 50 pulses per location. The corresponding crater cross-sections of the two samples are depicted in **Fig. 1b** and **d,** showing a crater diameter of 40 μm for both samples. An average laser sampling depth (or depth resolution) of 700 nm/pulse was determined as the ratio of the crater depth over the total number of laser pulses (50).

A typical fs-LIBS spectrum of LLZO is shown in **Fig. 2**, covering a spectral range of 45 nm per acquisition. Two distinct spectral ranges were selected to measure the atomic ratios of Al, Li and Zr over La: 390 to 403 nm and 452 to 500 nm. Time-resolved measurements were also performed to ensure that the entire lifetime of the spectral

emission was captured in every acquisition. The ICCD gate width and delay were optimized to maximize the signal-to-noise ratio at 500 ns and 80 ns respectively. **Fig. 2** shows in blue the LIBS emission lines of Al I (396.2 nm), Li I (460.3 nm), La I (401.5 nm, 495.0 nm) and Zr I (468.8 nm) that were used for analysis. In addition to these elements, Ca ionic lines at 396.8 nm were measured in the LIBS spectra of the two LLZO samples, possibly resulting from contamination by furnace insulating parts.

3.2 Determination of Li/La, Zr/La and Al/La ratios

The bulk atomic ratio of Al:Li:La:Zr for LLZO_0h was measured as 0.31:5.27:3:1.96 from ICP-OES measurements. Deviation from the targeted Al:Li:La:Zr 0.3:6.1:3:2 ratio ($Li_{6.1}Al_{0.3}La_3Zr_2O_{12}$) in the case of Li has been attributed to the evaporation of the alkali metal at elevated temperatures during sample preparation.[33]

The mean Li/La, Zr/La and Al/La intensity ratios of each lateral layer were studied as a function of number of laser pulses (or depth) revealing the existence of a plateau (i.e. after approximately 15 laser pulses or 10.5 μm from the surface for Al/La) (**Fig. 3**). The stabilized atomic ratio intensities were averaged and used as representative intensity ratios matching the atomic ratios measured with ICP-OES. The error bars represent the standard deviation from the mean intensity ratio in each lateral layer.

3.3 Layer-by-layer contour maps

Fig.4 shows layer-by-layer contour maps of the Li/La (**a,d**), Zr/La (**b,e**) and Al/La (**c,f**) atomic ratios for the two LLZO samples. Each layer represents an 1110×1110 μm^2 area. Due to the use of two spectral ranges, the Li/La and Zr/La maps were produced from the same sample area while the Al/La information was acquired from an area nearby. These maps demonstrate the variations in the atomic ratios within each layer and are a result of combining the locations and depths, to provide information on the compositional gradients from the sample top surfaces to interiors. For clarity, contour maps of only eight layers are shown, and represent the atomic ratio distributions at the following depths from the surface: 0.7, 1.4, 2.1, 2.8, 3.5, 7, 21, and 35 μm. Non-uniform atomic ratio distributions are evident both in the lateral and vertical planes in agreement with previous

EDS and XRD reports,[6,34] and has often been associated with loss of lithium at the grain boundaries and the formation of impurity phases (e.g., $LaAlO_3$, $La_2Zr_2O_7$).[35]

A detailed description of the level of homogeneity of the chemical distribution is presented in the form of histograms. **Fig.5** depicts the percentage (%) of area coverage as a function of atomic ratio per layer. The Al/La and Li/La distributions for the two samples are shown in **Fig.5a,b** and **Fig.5c,d,** respectively. The width and symmetry of these distributions is indicative of the sample homogeneity; narrow and symmetric plots represent homogeneous compositional distributions. The Al/La ratio of LLZO_0h (**Fig. 5a**) exhibits a wide distribution that is slightly shifted towards higher Al/La ratios for the first few micrometers from the surface. This distribution is stabilized with depth (e.g. for 17.5 and 35.0 μm from the surface). On the contrary, the Al/La distribution of LLZO_6h is significantly broader at a depth of 1.4 μm and shifted towards even larger Al/La ratios, which represent a highly Al-rich layer (**Fig. 5b**).

The Li/La ratio distribution for both samples also varies at different depths, as shown in **Fig. 5c** and **d**, but the distribution is similar for two samples at the same depths. There appears to be lithium enrichment close to the surfaces, although the distribution is more widespread than deeper in the samples, where lithium is more uniformly distributed. This is consistent with the formation of Li_2CO_3 on sample surfaces. The presence of Li_2CO_3 on LLZO samples exposed even for brief periods of time to air has been observed by synchrotron x-ray photoemission spectroscopy (XPS) and soft X-ray absorption spectroscopy (sXAS), and is the cause of high Li/LLZO interfacial impedances.[10,11]

3.4 Cross-sectional maps

The cross-sectional contour maps for the two samples are shown in **Fig.6**. These cross-sections (**Fig.6 a-f**) include detailed atomic ratio information from all 50 layers across a single axial section. The distributions of Li/La, Zr/La and Al/La are plotted together with the mean atomic ratio as a function of depth in **Fig.6 g-i**.

The Li/La atomic ratio for the first 1.4 μm exceeds 2.6 for both samples, a value higher than the theoretically predicted ratio of 2.03 for the starting materials (Li:La=6.1:3). Surface enrichment of Li is consistent with formation of Li_2CO_3 upon pellet exposure to

air,[12] as observed in the layer-by layer contour maps over the first few micrometers from the surface.

The Zr/La ratio of both LLZO_0h and LLZO_6h is similar and remains fairly constant, with the exception of a marginal enrichment in the first 2.1 μm from the surface. This observation is in agreement with previous surface and cross-section EDS studies that revealed similar Zr/La atomic ratios on the surface and in the bulk of LLZO pellets.[36]

The Al/La atomic ratio of LLZO_0h also remains fairly constant as a function of depth. A small increase (~14% over mean value) in the Al/La atomic ratio is observed at for the first 1.4 μm from the surface, and marginally increases at depths from 2.8 to 21 μm. $La_2Li_{0.5}Al_{0.5}O_4$ has been observed on LLZO surfaces,[9] including samples similar to these,[7] and may be responsible for the slight Al enrichment near the surfaces of this sample observed in the LIBS experiment. In contrast, the Al/La ratio in LLZO_6h is much higher close to the surface. For this sample, the high Al/La intensity at top layers to 2.1 μm likely reflects the lateral distribution of $LaAlO_3$ and $LiAlO_2$ impurities in the grain boundaries because the lateral displacement is approximately 150 μm, similar to the grain size.[9] Densifying the LLZO pellet under a pre-annealed cover powder as was done for LLZO_6h resulted in a 10% higher Al content that for LLZO_0h, which was covered with fresh powder. Energy dispersive x-ray spectroscopy showed that the excess Al concentrated in the grain boundaries.[9]

The presence of Al-rich areas has been reported in LLZO samples with EDS and XRD. The $LaAlO_3$ phase has been known to occur as the Al concentration increases,[7,35] and can lead to a substantial increase of the Al/La ratio compared to that of the starting material (i.e. ratio of 0.14 in this study . Contamination originating from Al_2O_3 crucibles can also lead to localized Al-enrichment of the LLZO surface or the grain boundaries where Al^{3+} enters the polycrystalline sample.[11,35]

3.5 Visualization of 3D chemical distribution

Visualization of elemental distribution becomes more elaborate as the number of data points per element increases. For example a total of 11,250 data points/atomic ratio were acquired per sample presented in this work. 2D layer-by-layer cannot be used to adequately present the material matrix (e.g., **Fig.4** where only a few out of 50 layers are

shown). As a result, extended visualization capabilities are required to address the dimensionality of the problem.

For 3D elemental visualization, color-coding, voxel definition and density dependent opacity were combined. Voxel, short for volume pixel refers to the smallest distinguishable box-shaped part of a three-dimensional image. Stacks of 2D cross-sectional elemental ratio maps (depth) were produced for every element of interest and served as volumetric datasets. These datasets were used to add depth to an image (voxelization). In 3D imaging, voxels must further undergo opacity transformation, a procedure that provides voxels different transparency values based on their individual values. This transformation exposes interior details of an image that would otherwise be concealed by darker and more opaque outer-layer voxels. These visualization methods were adopted to create merged overlays of multiple elements in 3D.

The spatial distributions of the atomic ratios are shown as individual images (**Fig.7a-c** and **Fig.7e-g**) and as merged overlays in **Fig.7d,h** with colours corresponding to the following ratios: Al/La-blue, Li/La-green, Zr/La-red. The scale bar is 1.1 mm × 1.1 mm ×35 μm, and each voxel size is 74×74×0.7 μm. A linear colour scale was used in the 3D rendering of the atomic ratios, with the brightest colours representing the highest intensities. These images represent three-dimensional distributions viewed under 60 deg rotation across the horizontal (x-) axis. By merging the ratios of Li/La and Zr/La (**Fig.7d,h**), the correlation between the two atomic ratio distributions is directly demonstrated.

The 3D chemical maps of two LLZO samples reveal that they have very similar bulk chemical compositions, but different compositions in first few micrometers from the surface. The differences in elemental distribution are traced back to the material processing conditions, verifying that the cover powder critically affects the chemical reactions during the sample annealing process as well as the electrochemical performance of the system.[9,10]

Conclusions

3D multi-elemental mapping of the solid electrolyte material LLZO by fs-LIBS has been demonstrated for the first time. Atomic ratios of Al/La, Li/La, Zr/La and Al/La were

determined in a 3D space of $1.11 \times 1.11 \times 0.035$ mm^3 with 74 μm lateral and 700 nm depth resolution. Variations in the elemental distributions and atomic ratios of Li/La and Al/La were observed for LLZO pellets prepared different ways. Surface Al-enrichment was more pronounced for LLZO densified under an annealed powder cover than for LLZO processed under fresh powder and is consistent with observations of Al-rich impurities at grain boundaries observed in previous studies on similar samples. Surface lithium enrichment was observed in both cases, attributable to the formation of Li_2CO_3 during brief air exposures. The ability of fs-LIBS to directly image elements in 3D allows a sophisticated understanding of the distribution of impurities, which can govern the electrochemical behaviour of solid electrolytes, and are not easily observed by other conventional characterization techniques.

Acknowledgements

This research has been supported by the Chemical Science Division, Office of Basic Energy Sciences, and the Assistant Secretary for Energy Efficiency and Renewable Energy, Office of Vehicle Technologies of the U.S. Department of Energy under contract no. DE-AC02-05CH11231. This work was also supported by Small Business Innovation Research (SBIR) funding through Applied Spectra Inc., and Laboratory Directed Research and Development (LDRD) funding from Berkeley Lab, provided by the Director, Office of Science, of the U.S. Department of Energy. Huaming Hou would like to thank the Innovation and Research Foundation of the Ocean University of China and the China Scholarship Council. Dr Joong Sun Park and Professor Jordi Cabana are cordially acknowledged for helpful discussions.

recommendation, or favoring by the United States Government or any agency thereof, or the Regents of the University of California. The views and opinions of authors expressed herein do not necessarily state or reflect those of the United States Government or any agency thereof or the Regents of the University of California.

References:

1. P. Knauth, *Solid State Ionics*, 2009, **180**, 911–916.
2. R. Murugan, V. Thangadurai, and W. Weppner, *Angew. Chemie Int. Ed.*, 2007, **46**, 7778–7781.
3. J. Awaka, N. Kijima, H. Hayakawa, and J. Akimoto, *J. Solid State Chem.*, 2009, **182**, 2046–2052.
4. C. a Geiger, E. Alekseev, B. Lazic, M. Fisch, T. Armbruster, R. Langner, M. Fechtelkord, N. Kim, T. Pettke, and W. Weppner, *Inorg. Chem.*, 2011, **50**, 1089–1097.
5. H. Buschmann, J. Dölle, S. Berendts, A. Kuhn, P. Bottke, M. Wilkening, P. Heitjans, A. Senyshyn, H. Ehrenberg, A. Lotnyk, V. Duppel, L. Kienle, and J. Janek, *Phys. Chem. Chem. Phys.*, 2011, 13, 19378–19392.
6. E. Rangasamy, J. Wolfenstine, J. Allen, and J. Sakamoto, *J. Power Sources*, 2013, **230**, 261–266.
7. Y. Jin and P. J. McGinn, *J. Power Sources*, 2011, **196**, 8683–8687.
8. Y. Li, J.-T. Han, C.-A. Wang, S. C. Vogel, H. Xie, M. Xu, and J. B. Goodenough, *J. Power Sources*, 2012, **209**, 278–281.
9. L. Cheng, J. S. Park, H. Hou, V. Zorba, G. Chen, T. Richardson, J. Cabana, R. Russo, and M. Doeff, *J. Mater. Chem. A*, 2014, **2**, 172–181.
10. L. Cheng, E. J. Crumlin, W. Chen, R. Qiao, H. Hou, S. Franz Lux, V. Zorba, R. Russo, R. Kostecki, Z. Liu, K. Persson, W. Yang, J. Cabana, T. Richardson, G. Chen, and M. Doeff, *Phys. Chem. Chem. Phys.*, 2014, **16**, 18294–18300.
11. L. Cheng, W. Chen, M. Kunz, K. Persson, N. Tamura, G. Chen, and M. Doeff, *Appl. Mater. Interfaces*, 2015, **7**, 2073–2081.
12. Y. Li, J.-T. T. Han, C.-A. A. Wang, H. Xie, and J. B. Goodenough, *J. Mater. Chem.*, 2012, **22**, 15357–15361.

13. J. Wolfenstine, J. Sakamoto, and J. L. Allen, *J. Mater. Sci.*, 2012, **47**, 4428–4431.

14. M. Dong, D. Oropeza, J. Chirinos, J. J. Gonz âlez, J. Lu, X. Mao, and R. E. Russo, *Spectrochim. Acta Part B At. Spectrosc.*, 2015, **109**, 44–50.

15. M. Dong, X. Mao, J. J. Gonzalez, J. Lu, and R. E. Russo, *J. Anal. At. Spectrom.*, 2012, **27**, 2066–2075.

16. X. Li, Z. Wang, X. Mao, and R. E. Russo, *J. Anal. At. Spectrom.*, 2014, **29**, 2127–2135.

17. B. Y. Cai, X. Mao, H. Hou, V. Zorba, R. E. Russo, and N.-H. Cheung, *Spectrochim. Acta Part B At. Spectrosc.*, 2015, **110**, 51–55.

18. Q. L. Ma, V. Motto-Ros, W. Q. Lei, M. Boueri, L. J. Zheng, H. P. Zeng, M. Bar-Matthews, A. Ayalon, G. Panczer, and J. Yu, *Spectrochim. Acta Part B At. Spectrosc.*, 2010, **65**, 707–714.

19. K. Novotný, J. Kaiser, M. Galiová, V. Konečná, J. Novotný, R. Malina, M. Liška, V. Kanick ý, and V. Otruba, *Spectrochim. Acta Part B At. Spectrosc.*, 2008, **63**, 1139–1144.

20. J. Kaiser, M. Galiová, K. Novotný, R. Červenka, L. Reale, J. Novotný, M. Liška, O. Samek, V. Kanický, A. Hrdlička, K. Stejskal, V. Adam, and R. Kizek, *Spectrochim. Acta Part B At. Spectrosc.*, 2009, **64**, 67–73.

21. W. Wessel, A. Brueckner-Foit, J. Mildner, L. Englert, L. Haag, A. Horn, M. Wollenhaupt, and T. Baumert, *Eng. Fract. Mech.*, 2010, **77**, 1874–1883.

22. J. R. Chirinos, D. D. Oropeza, J. J. Gonzalez, H. Hou, M. Morey, V. Zorba, and R. E. Russo, *J. Anal. At. Spectrom.*, 2014, **29**, 1292–1298.

23. C. D. Quarles, J. J. Gonzalez, L. J. East, J. H. Yoo, M. Morey, and R. E. Russo, *J. Anal. At. Spectrom.*, 2014, **29**, 1238.

24. D. W. Hahn and N. Omenetto, *Appl. Spectrosc.*, 2012, **66**, 347–419.

25. D. W. Hahn and N. Omenetto, *Appl. Spectrosc.*, 2010, **64**, 335A–366A.

26. O. Samek, V. Margetic, and R. Hergenr öder, *Anal. Bioanal. Chem.*, 2005, **381**, 54–56.

27. B. N. Chichkov, C. Momma, S. Nolte, F. Alvensleben, and A. T ünnermann, *Appl. Phys. A*, 1996, **63**, 109–115.

28. A. H. Galmed, A. K. Kassem, H. Bergmann, and M. A. Harith, *Appl. Phys. B*, 2010, **102**, 197–204.

29. V. Zorba, J. Syzdek, X. Mao, R. E. Russo, and R. Kostecki, *Appl. Phys. Lett.*, 2012, **100**, 234101.

30. V. Zorba, X. Mao, and R. E. Russo, *Anal. Bioanal. Chem.*, 2010, **396**, 173–180.

31. D. J. Hwang, H. Jeon, C. P. Grigoropoulos, J. Yoo, and R. E. Russo, *Appl. Phys. Lett.*, 2007, **91**, 251118.

32. Y. Lu, V. Zorba, X. Mao, R. Zheng, and R. E. Russo, *J. Anal. At. Spectrom.*, 2013, **28**, 743–748.

33. I. Kokal, M. Somer, P. H. L. H. L. Notten, and H. T. T. Hintzen, *Solid State Ionics*, 2011, **185**, 42–46.

34. K. Chen, M. Huang, Y. Shen, Y. Lin, and C. W. Nan, *Solid State Ionics*, 2013, **235**, 8–13.

35. E. Rangasamy, J. Wolfenstine, and J. Sakamoto, *Solid State Ionics*, 2012, **206**, 28–32.

36. J. Tan and A. Tiwari, *Electrochem. Solid-State Lett.*, 2012, **15**, A37–A39.

List of Figures

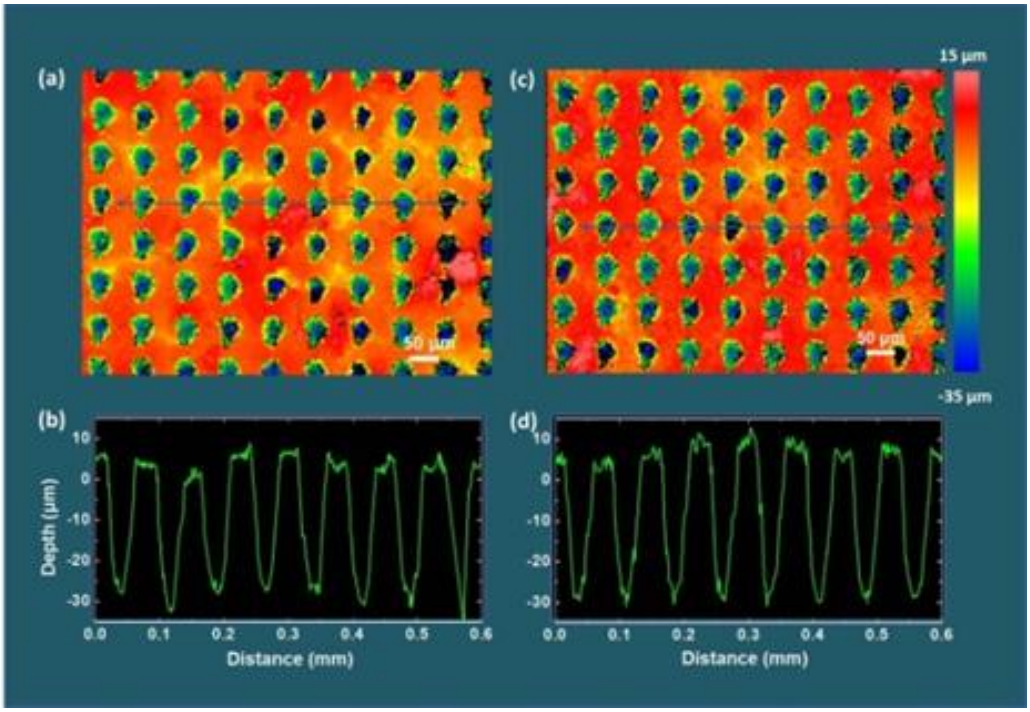

Fig.1 White light interferometry surface maps of the laser-sampled areas for (a) LLZO_0h and (c) LLZO_6h. (b), (d) corresponding line profiles of the craters across the horizontal blue lines shown in (a) and (c).

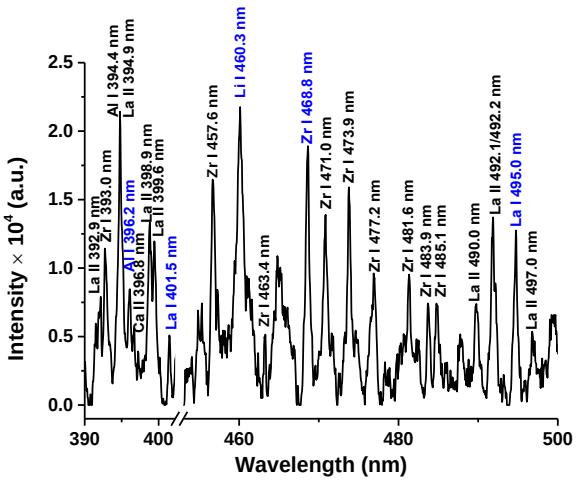

Fig.2 Representative LIBS spectral emission from LLZO_0h. The spectral lines used for atomic ratio calculation and mapping purposes are shown in blue.

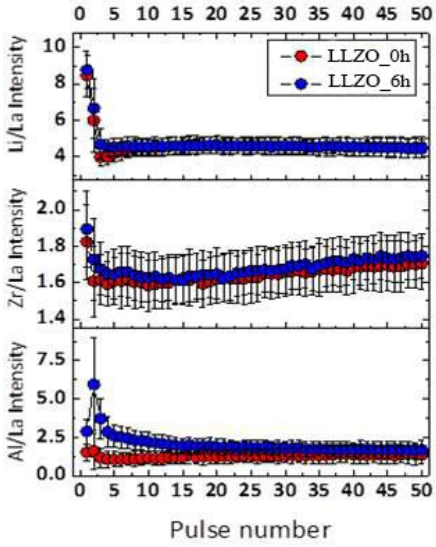

Fig.3 Intensity ratios of the Li I 460.3 nm/La I 495.0 nm (top), Zr I 468.8 nm/La I 495.0 nm (middle) and Al I 396.2 nm/La I 401.5 nm (bottom) LIBS peaks as functions of number of laser pulses.

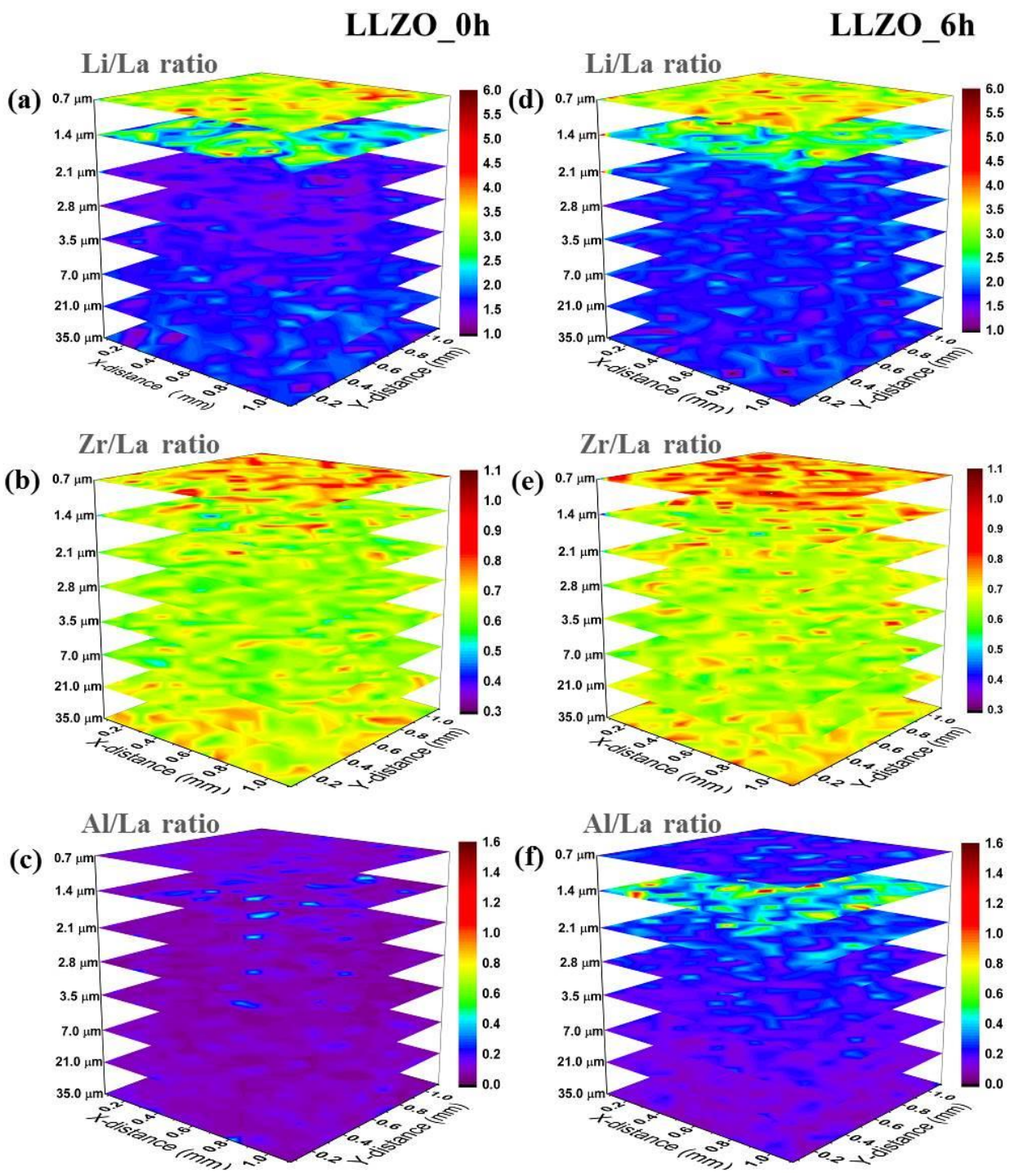

Fig.4 Atomic ratios for major and minor elements in two LLZO pellets prepared under different conditions, for the first 35 µm from the surface. a) Li/La, b) Zr/La and c) Al/La ratios for LLZO_0h. d) Li/La, e) Zr/La and f) Al/La ratios for LLZO_6h. The depth/pulse is 700 nm (total sampled area/layer: 1.11 mm x 1.11 mm). Al-rich areas are found at the surface (0.7 to 2.1 µm in depth) of LLZO_6h (f).

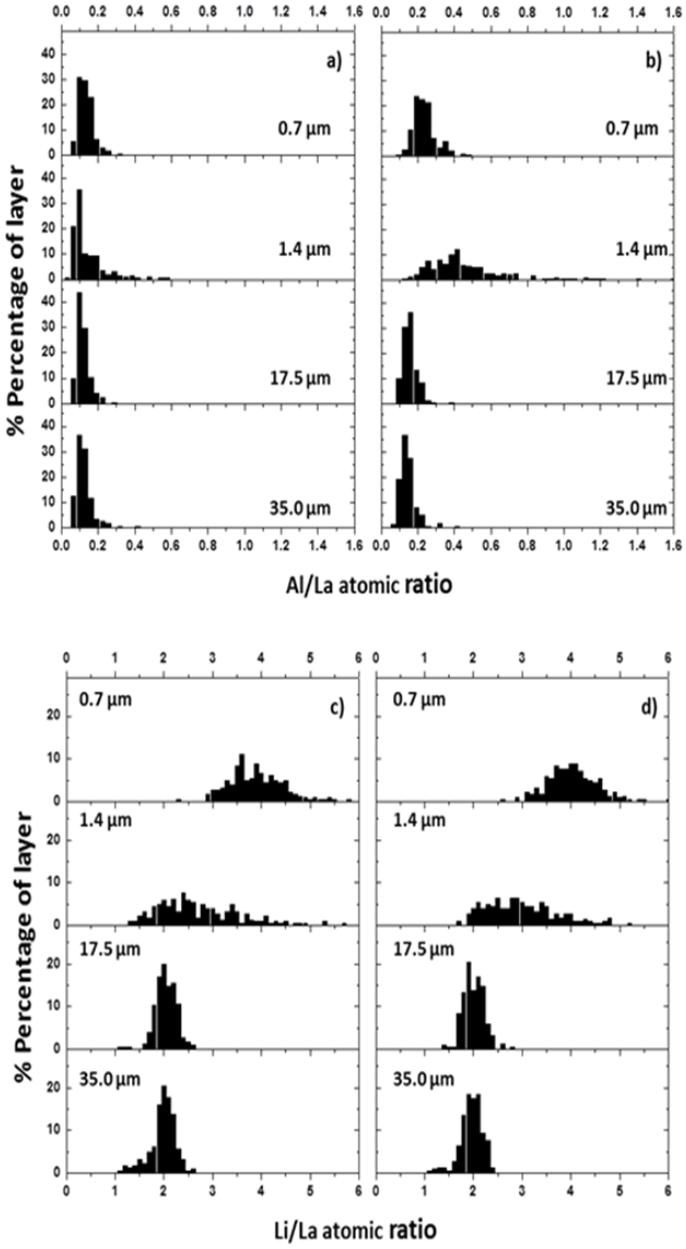

Fig.5 Distributions of atomic ratio across selected layers depths from the sample surface (0.7, 1.4, 17.5, 35.0 µm). The atomic ratio of Al/La is shown in a) for LLZO_0h and b) for LLZO_6h. The Li/La atomic ratio is shown in c) and d) for LLZO_0h and LLZO_6h respectively.

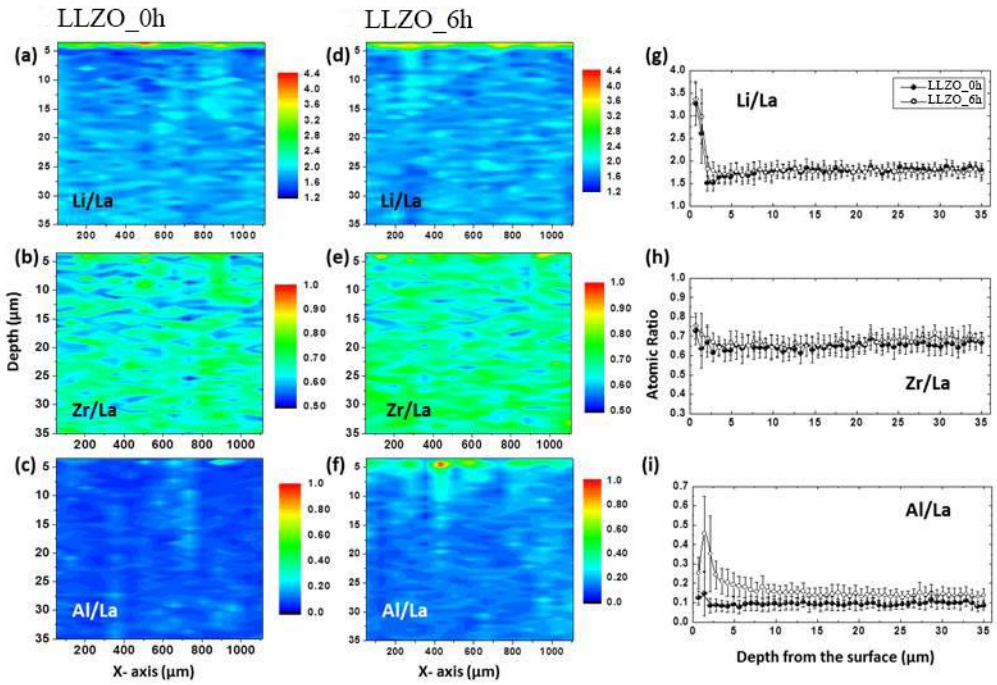

Fig.6 Atomic ratio (Li/La, Zr/La, Al/La) maps as a function of depth across a section of the two LLZO samples (a-f), and mean atomic ratio as a function of depth (g-i). The error bars represent the standard deviation in the atomic ratios across each lateral plane.

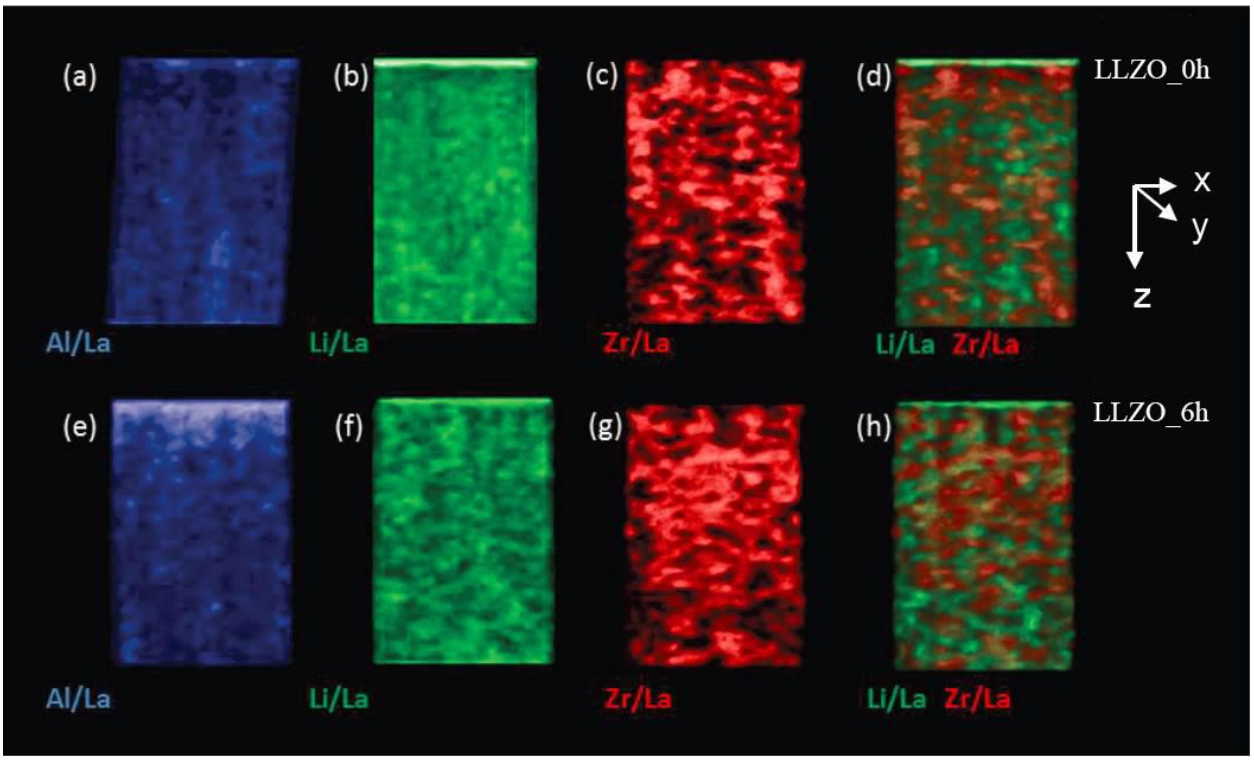

Fig.7 Computational conversion of the spatially resolved LIBS data allows reconstruction of the distribution of different elements and relative ratios in 3D across different planes and viewing angles. Colours correspond to the following ratios: Al/La-blue, Li/La-green, Zr/La-red. The ratios for samples LLZO_0h and LLZO_6h are shown in a-d and e-h, respectively. Here the plots are viewed under 60 deg rotation across the horizontal (x-) axis.